



## Pyrolysis-based modelling of 18650-type lithium-ion battery fires in thermal runaway with LCO, LFP and NMC cathodes

Hosein Sadeghi, Francesco Restuccia\*

Department of Engineering, King's College London, Strand, London, WC2R 2LS, UK



### HIGHLIGHTS

- Pyrolysis models were generated for thermal runaway simulations of 18650-type LIB.
- The models result in experimentally verified flame heat release rates.
- Maximum soot yields were  $5.7 \times 10^{-8}$  (LCO),  $1.6 \times 10^{-8}$  (LFP) and  $4.1 \times 10^{-9}$  (NMC).
- Radiative flux to surroundings was 10 times greater than on cell surface.
- The maximum and minimum flame height were 0.62 m and 0.29 m, respectively.

### ARTICLE INFO

**Keywords:**  
Pyrolysis modelling  
Thermal runaway modelling  
Lithium-ion battery  
18650-type battery  
Flame height  
Radiative heat flux

### ABSTRACT

This study presents a modelling approach for simulating fires in thermal runaway and here, it is applied to 18650-type batteries with LCO, NMC, and LFP cathodes at 100% SOC. The model assumes a single-step pyrolysis, where a solid lumped substance, representing the battery components, degrades into volatiles which are vent gases here. Coupling an in-house MATLAB code and FDS solver, a parameter estimation using Bayesian optimization was performed to fit the simulated mass loss and heat release rate to the experimental measurements. One-step kinetics are used for vent gas combustion, with CO yield obtained from literature and soot yield determined via 1-D diffusion flame simulations with CRECK kinetic mechanism in Cantera solver. 3-D simulations using the obtained models yielded maximum values of flame temperature,  $\text{CO}_2$  and  $\text{H}_2\text{O}$  mole fractions, velocity, radiative heat flux, and flame height as 2520 K, 0.47, 0.15, 10.08 m/s, 13.29 kW/m<sup>2</sup>, and 0.62 m, respectively. The novelties associated with this approach are that, unlike the past studies, there is no need to model the thermal runaway process prior to flaming and, the resulting heat release rate is experimentally verified which makes further analyses, such as flame temperature, height and heat emissions possible.

### 1. Introduction

Since the invention of LIB, their use has been widespread. The applications of LIBs can be categorized into three main groups: consumer electronics, motor vehicles and grid storage. They offer a high energy density, are lightweight and have a long lifespan. However, safety is still a significant challenge due to the fire risks. The main components of an LIB are cathode, anode, separator, and electrolyte. The cathode is made of transition metal oxides such as  $\text{LiCoO}_2$  (LCO),  $\text{LiMn}_2\text{O}_4$  (LMO),  $\text{Li}(\text{Ni}_\alpha\text{Co}_\beta\text{Al}_\gamma)\text{O}_2$  (NCA),  $\text{Li}(\text{Ni}_\alpha\text{Mn}_\beta\text{Co}_\gamma)\text{O}_2$  (NMC) and  $\text{LiFePO}_4$  (LFP) [1]. During past years, the most widely used cathode has been LCO [2], however, high energy density of NMC and the long cycle life of LFP make

them favourable for electrochemical energy storage systems (ESS) and electric vehicles (EV) [3]. The anode material is commonly made from graphite, due to its high energy density or  $\text{Li}_4\text{Ti}_5\text{O}_{12}$  (LTO) for better cycle performance at high temperature and better thermal stability. However, newly introduced materials such as silicon, tin, antimony and germanium have specific applications based on their properties [1]. The cathode and anode are detached with a separator to prevent internal short circuit (ISC) while allowing lithium ions to transfer freely. The conventional material for the separator is polyolefin membranes made from polyethylene or polypropylene [1]. Commonly made of an organic carbonate solvent and  $\text{LiPF}_6$ , the electrolyte is used to fill the porous space of the separator and electrodes which enables lithium ions transfer between cathode and anode during charge and discharge.

\* Corresponding author.

E-mail address: [francesco.restuccia@kcl.ac.uk](mailto:francesco.restuccia@kcl.ac.uk) (F. Restuccia).

<b>Nomenclature</b>	
<i>A</i>	Pre-exponential factor [ $s^{-1}$ ]
<i>c<sub>p</sub></i>	Specific heat [ $\text{kJ kg}^{-1}\text{K}^{-1}$ ]
<i>E</i>	Activation energy [ $\text{J mol}^{-1}$ ]
<i>f<sub>v</sub></i>	Soot volume fraction [-]
$\Delta h_c$	Heat of combustion [ $\text{kJ kg}^{-1}$ ]
$\Delta h_r$	Heat of reaction [ $\text{kJ kg}^{-1}$ ]
<i>i</i>	Index of material [-]
<i>j</i>	Index of reaction [-]
<i>k</i>	Thermal conductivity [ $\text{W m}^{-1}\text{K}^{-1}$ ]
<i>Ma</i>	Mach number [-]
<i>m</i>	Mass [kg]
<i>n</i>	Reaction order [-]
<i>q"</i>	Heat flux [ $\text{kW m}^{-2}$ ]
<i>R</i>	Universal gas constant [ $\text{kJ mol}^{-1}\text{K}^{-1}$ ]
<i>R</i>	Radiative heat flux ratio [-]
<i>T</i>	Temperature [K]
<i>t</i>	Time [s]
<i>W</i>	Molar weight [kg mol $^{-1}$ ]
<i>X</i>	Mole fraction [-]
<i>x,y,z</i>	Coordinates [m]
<i>Y</i>	Mass fraction [-]
<i>y<sub>CO</sub></i>	CO yield [-]
<i>y<sub>soot</sub></i>	Soot yield [-]
<i>Greek letters</i>	
$\gamma$	Residue mass fraction [-]
$\epsilon$	Emissivity [-]
$\rho$	Density [ $\text{kg m}^{-3}$ ]
<i>φ</i>	Equivalence ratio [-]
$\chi$	Mass loss or HRR [variable]
<i>Subscripts</i>	
<i>c</i>	Char
<i>f</i>	Fuel
<i>m</i>	Material
<i>o</i>	Oxidizer
<i>r</i>	Radiative heat flux
<i>s</i>	Solid
<i>st</i>	Stoichiometric
<i>surf</i>	Surface
<i>surr</i>	Surroundings
<i>Abbreviations</i>	
ARC	Accelerating Rate Calorimetry
CSBC	Copper Slug Battery Calorimetry
EV	Electric vehicle
FDS	Fire dynamics simulator
HRR	Heat release rate
ISC	Internal short circuit
LCO	Lithium cobalt oxide
LES	Large eddy simulation
LFP	Lithium ferrous phosphate
LIB	Lithium-ion battery
LMO	Lithium manganese oxide
LTO	Lithium titanium oxide
MAE	Mean absolute error
NMC	Nickel manganese oxide
PVC	Polyvinyl chloride
SOC	State of charge

Thermal runaway is a battery self-heating process which is the main cause of battery hazards. It is mainly due to mechanical, thermal or electrical abuse [1]. Nail puncture extrusion deformation, poor cooling system and overcharging/overdischarging are some of the examples [1, 4]. In thermal runaway, when the battery reaches a critical temperature, the internal components fail. The failures are associated with chemical reactions between the battery components leading to producing high-temperature flammable gases venting out from the battery (or battery safety valve) due to the high pressures. The vent gases may consist of CO<sub>2</sub>, H<sub>2</sub>, CO, C<sub>2</sub>H<sub>4</sub>, CH<sub>4</sub>, C<sub>2</sub>H<sub>6</sub>, C<sub>3</sub>H<sub>8</sub> and C<sub>3</sub>H<sub>6</sub> [3,5]. However, the amount of the species varies for every scenario and mainly depends on the cathode material and state of charge (SOC) [6]. Mixing with the environment's oxygen, these high-temperature gases eventually ignite and cause severe fires. The combustion and explosive characteristics of the vent gases have been studied in previous works as a premixed flame [6–10]. The studied characteristics included laminar burning velocity [6,8,9], combustion energy [10], explosion pressure [6, 8,11] and pressure rise rate [6,11]. These works mainly focused on the explosive hazards of the vent gases which emerge at the ignition time and threaten the confined battery cells and packs. After the ignition, the fire can last for minutes and lead to a complete failure of the system and subsequent hazards to the surroundings. This stage can be studied as diffusion combustion. From this point of view, measurement of some parameters such as vent gas temperature, combustion heat release rate (HRR) [12,13], combustion products, battery surface temperature [12–15], flame temperature [16], and heat and toxic gas emissions [13] are prominent. The measurements were conducted in different ways such as Cone Calorimetry [12,13], Copper Slug Battery Calorimetry (CSBC) [14], and Accelerating Rate Calorimetry (ARC) [15]. The experiments showed that the behaviour of the battery fire and the hazards, firstly, depend on SOC [12–15], cathode material [17] and secondly, are

affected by environment pressure [18], environment oxygen content [19], incident heat flux to the cell [20] and heating mechanism [21].

So far, the numerical modelling of the thermal runaway of an 18650-type cell has been carried out in two ways: with (e.g. Refs. [16,22]) and without (e.g. Ref. [11]) considering the flame. Including the flame, Kim et al. [22] proposed a model by coupling the thermal abuse reactions and fluid dynamics and they studied cell venting, cell internal pressure and gas-phase dynamics. In Ref. [22], the venting events were classified into two stages: first the internal pressure rise and second, venting of the gases, while the first stage had a very negligible effect on the propensity for propagation [22]. Kong et al. [16] developed a model to predict the thermal abuse reactions, gas phase dynamics and combustion of the vent gases in order to consider the effects of jet fire and different modes of heat transfer in LIB fires. Takagishi et al. [23] conducted a 3-D simulation considering joule heating, thermal decomposition reactions, gas-phase dynamics and combustion. They studied a single cell and a battery module and reported the battery voltage behaviour, vent gas velocity, cell pressure and cell temperature at different stages of thermal runaway. Including particle ejection, Zhang et al. [24] reported the contribution of the particles to flame heat flux emissions.

As reviewed, the modelling studies primarily concentrated on solid-phase properties such as cell temperature. The studies that have included gas-phase combustion have employed complex methodologies, including the coupling of heat generation in the cell with computational fluid dynamics [16,22], making their replication by other researchers a challenging endeavour. Even having the model replicated by coupling several solutions, the important flame properties, such as heat release rate, are not verified against experimental measurements. As shown in Ref. [23], since the combustion reactions of the vent gases are complex, it is difficult to directly model the heat release rate of the flame. In this context, novel methodologies are required for studying battery fires

during thermal runaway.

This study seeks to address this gap by introducing pyrolysis-based models for simulations of the 18650-type battery flames in thermal runaway. The term “pyrolysis-based” is used because the fundamental concept parallels pyrolysis modelling in fire science (e.g. Refs. [25,26]). In other words, the solid material undergoes degradation, generating flammable volatiles that lead to low-Mach thermally driven flames. Instead, here, the battery materials undergo pyrolysis, and the flammable volatiles are battery vent gases, exhibiting turbulent jet dynamics. Additionally, in conventional pyrolysis modelling, the materials are well-characterized. However, in the present study, the intricate materials of a LIB are replaced with a single unknown material, which could potentially result in the use of non-physical properties. These models avoid the need for coupling multiple solutions, i.e., heat generation, gas accumulation, jet flow and combustion. More importantly, the current approach results in experimentally verified heat release rate of the flame, which is the main novelty of the present work, allowing the resulting flame properties to be used for further analysis of thermal runaway conditions.

The models were generated for batteries with LCO, NMC and LFP cathodes due to their wide range of applications [3]. The 100% SOC was considered here as it is prone to higher fire risks compared to lower SOCs [22,27] due to the higher number of unstable ions at this state [21]. The modelling process involved fitting the mass loss and heat release rate values to the experimental measurements through an iterative optimization with parameter estimation process by coupling FDS (Fire Dynamics Simulator) and MATLAB. Furthermore, the soot yields for the flames with each cathode material were determined by solving a 1-D diffusion flame with CRECK kinetic mechanism [28] using Cantera solver. Then, the scalar fields of the gaseous species and the flame temperature, flame height and radiative heat fluxes reaching the battery surface and surroundings were studied through 3-D simulations with FDS. Concisely, this study encompasses the following key subjects:

- 1 Pyrolysis modelling of 18650-type lithium-ion battery cells for thermal runaway simulations (using MATLAB-FDS coupling).
- 2 Calculating soot yields to predict emissions in thermal runaway (using Cantera).
- 3 Determining flame properties such as scalar fields, flame height and radiative heat flux to predict potential hazards to the surroundings and thermal runaway propagation (using FDS).

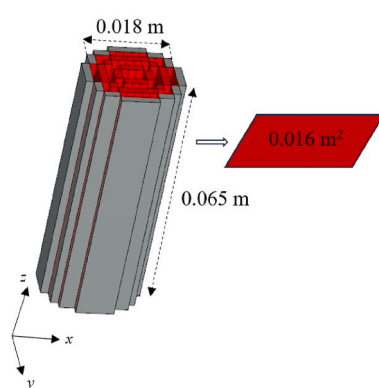


**Fig. 1.** The geometry of the battery cell with the pyrolysis surfaces shown in red (left), and the representative pyrolysis surface (right). (For interpretation of the references to colour in this figure legend, the reader is referred to the Web version of this article.)

## 2. Methodology

### 2.1. Model setup

In this work, flaming of a single 18650-type LIB cell in thermal runaway was modelled. Fig. 1 shows the geometry of the battery. As shown, the battery was assumed to be laterally layered to represent the actual jelly roll, rather than a simple cube. Here, the positive cap was neglected to allow the vent gases to eject from the top and the flame to propagate vertically, as suggested in Refs. [11,16]. The pyrolysis process was assumed to occur on the inner surfaces of the cell (shown in red) with a total surface area of  $0.016 \text{ m}^2$ . This area is optional and was found after making the geometry and then was used as the area of the representative pyrolysis surface in the next sections.

### 2.2. Governing equations

The battery thermal runaway was assumed to initiate as a pyrolysis process generating flammable gases, as the battery vent gases, and a residue representing the remaining solid materials after thermal runaway, similar to char for organic materials. The modelling was performed with the open-source FDS 6.7.9 solver. In this solver, the reaction mechanisms and reaction rates for the solid materials can be defined. For a non-oxidative reaction  $j$  of material  $i$ , the reaction rate at temperature  $T_s$  is defined as

$$r_{ij} = A_{ij} Y_{s,i}^{n_{s,ij}} \exp\left(\frac{E_{ij}}{RT_s}\right) \quad (1)$$

where  $A_{ij}$  is pre-exponential factor,  $Y_{s,i}$  is mass fraction of material  $i$ ,  $n_{s,ij}$  is the reaction order,  $E_{ij}$  is the activation energy and  $R = 8.314E - 3 \text{ kJ mol}^{-1} \text{ K}^{-1}$  is the universal gas constant. The mass fraction of material  $i$  is defined as

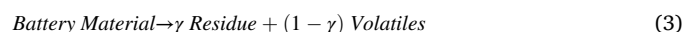
$$Y_{s,i} = \frac{\rho_{s,i}}{\rho_s(0)} \quad (2)$$

where  $\rho_{s,i}$  is the density of solid material  $i$  and  $\rho_s(0)$  is the initial density of the material layer. Then, the volatile is released at the first gas cell next to the pyrolysis surface without mass transfer resistance. For the gas phase, FDS solves low-Mach ( $Ma < 0.3$ ) LES equations for thermally driven flows which also is capable to solve for higher Mach numbers with no significant errors [29]. The governing equations are presented in the Supplementary Material, Appendix A.

## 3. Modelling

### 3.1. Pyrolysis modelling

Here, a pyrolysis modelling procedure similar to what carried out for PVC [25] and wood [26] was followed. To this end, a single-layer solid surface representing the battery internal components (called battery material here) with a single reaction were assumed, i.e.,  $i = j = 1$ . This representative surface is shown in Fig. 1. It was assumed here that the battery material underwent a decomposition process as



where  $\gamma$  is residue mass fraction. The residue was assumed to be non-reacting char and the vent gases were considered as volatiles here. The components of the vent gases for each cathode were obtained from the experimental measurements of Golubkov et al. [5] and are presented in Table 1. Here, according to the default FDS, the gas-phase combustion occurred when the fuel met the oxidizer without having an external source of heat (section 15 of FDS user guide [30]).

In pyrolysis modelling, the kinetic parameters of the reaction scheme are not known. Furthermore, in the present study, the properties of the

**Table 1**

Components of the battery vent gases with LCO, NMC and LFP cathodes at 100% SOC [5].

Cathode	Vent gas components [%]					
	C <sub>2</sub> H <sub>6</sub>	C <sub>2</sub> H <sub>4</sub>	CH <sub>4</sub>	CO	CO <sub>2</sub>	H <sub>2</sub>
LCO	1.2	7.7	8.6	27.6	24.9	30.0
LFP	0.3	6.8	4.1	4.8	53.0	30.9
NMC	0	8.2	6.8	13.0	41.2	30.8

hypothetical battery material were also unknown. These parameters are usually obtained in a parameter optimization process, which is the main task in pyrolysis modelling. Here, to simplify the parameter estimation, the reaction order in Eq. (1) was set at  $n_s = 1$ . Since this work studies the post-thermal runaway flame, the actual mass of the battery cell and its electrochemical degradation were not of interest. The parameter estimation was run for activation energy ( $E$ ), pre-exponential factor ( $A$ ), heat of reaction ( $\Delta h_r$ ), heat of combustion ( $\Delta h_c$ ), material thermal conductivity ( $k_m$ ), residue thermal conductivity ( $k_c$ ), material density ( $\rho_m$ ), residue density ( $\rho_c$ ), internal battery heat generation ( $q'$ ), material emissivity ( $\varepsilon$ ), material specific heat ( $c_{p,m}$ ) and thickness. These parameters were estimated through a two-step process, elaborated upon as follows.

In the first step, a kinetic analysis was performed with FDS to estimate  $E$  and  $A$ . To this end, the battery mass fraction and mass loss rate versus time were fitted to the data in the literature. A limitation here was that there were a few works in the literature reporting mass loss of the whole cell. Two available studies are those of Liu et al. [17] and Said [31]. The data of [17] did not have enough temporal resolution and therefore, the data from Ref. [31] was used here. However, the mass loss and mass loss rates reported in Ref. [31] were analytically calculated and were not measured during the experiments. Besides, the heating rate, as a function of temperature and time, was not reported in Ref. [31]. However, the final cell temperature was found to be at 570 K [31] and this value was used in the current study. Based on the values reported in section 4 of [31], residue mass fractions ( $\gamma$ ) of 0.66, 0.96 and 0.66 were set in Eq. (3) with LCO, LFP and NMC cathodes, respectively.

In the second step, the rest of parameters including the material thermal properties were estimated by fitting the HRR to the experimental data available in the literature for 18650-type batteries. The experimental HRR data were obtained through calorimetry and different values were reported for every cathode material. Here, the HRRs measured for batteries with LCO, LFP and NMC cathodes were considered only and, in total, 26 HRR curves were obtained from Said [31], Chen et al. [12], Fu et al. [13] and Wang et al. [32]. Fig. 2 shows the HRRs.

As seen in Fig. 2, the HRRs span a wide range of values which can be due to the different experimental procedures and uncertainties. Therefore, in this study, the pyrolysis parameters were obtained for minimum, mean and maximum HRRs. The minimum and maximum HRRs were

chosen based on the curves in Fig. 2 and the mean HRR was achieved by averaging all the curves shown in Fig. 2 for every cathode. Table 2 presents the references from which the minimum and maximum HRRs were taken.

Then, the optimal values found in step one was used in a simple 3-D case. This case was made of 3, 3 and 3 cells in  $x$ ,  $y$  and  $z$  directions, respectively. The geometry is presented in Supplementary Material, Appendix A. By “simple case”, the authors mean that the representative surface shown in Fig. 1, which is a rectangular surface with area of 0.016 m<sup>2</sup>, was in the simple 3-D case and HRR analyses were conducted.

To perform steps one and two, an in-house MATLAB code was coupled with FDS to run the optimization in an iterative process. The Bayesian Optimization Algorithm of MATLAB was implemented for minimizing the mean absolute error (MAE), as the objective function here, defined as Eq 4

$$MAE = \frac{1}{N} \sum_{i=1}^N |\chi_{\text{exp},i} - \chi_{\text{pred},i}| \quad (4)$$

where  $\chi$  is mass loss or heat release rate, the subscripts “exp” and “pred” refer to the experimental and the predicted values, respectively, and 100 data points were considered here ( $N = 100$ ). The Bayesian algorithm is useful when the function in question is a black-box model, i.e., the variation of the objective function versus the parameters are not known. Here, it was assumed that FDS solver is the black-box model. For further details, the readers are referred to Pelikan et al. [33]. Fig. 3 summarizes the parameter estimation process and shows the final obtained results in steps one and two. The estimated parameters are reported in Table 3.

Notably, there exists a departure from the conventional pyrolysis modelling due to simplifying assumptions, potentially resulting in the generation of some non-physical parameter inputs. In such type of modelling in the past literature, some works encouraged the use of solely physical parameters [34], while others made use of some non-physical parameters where appropriately justified [25]. In this work, the non-physical parameters generated are heat of reaction ( $\Delta h_r$ ) and heat of combustion ( $\Delta h_c$ ) and this is because in the gas-phase combustion, the fuel components were taken from Ref. [5] while the heat release rates were taken from other references. Therefore,  $\Delta h_r$  and  $\Delta h_c$  were compulsorily tuned here to fit the heat release rates to the experimental

**Table 2**

The references from which the HRR curves were obtained.

Cathode <sub>HRR</sub>	Reference
LCO <sub>min</sub>	Chen et al. [12]
LCO <sub>max</sub>	Fu et al. [13]
LFP <sub>min</sub>	Said [31]
LFP <sub>max</sub>	Chen et al. [12]
NMC <sub>min</sub>	Wang et al. [32]
NMC <sub>max</sub>	Said [31]

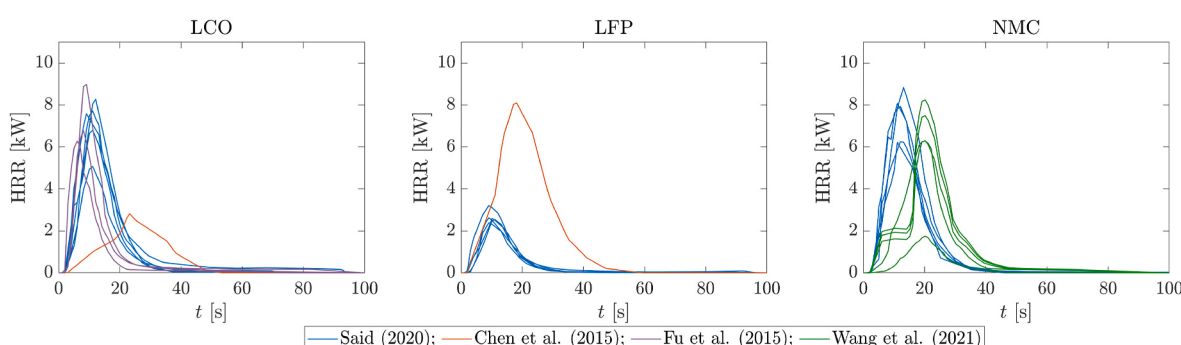
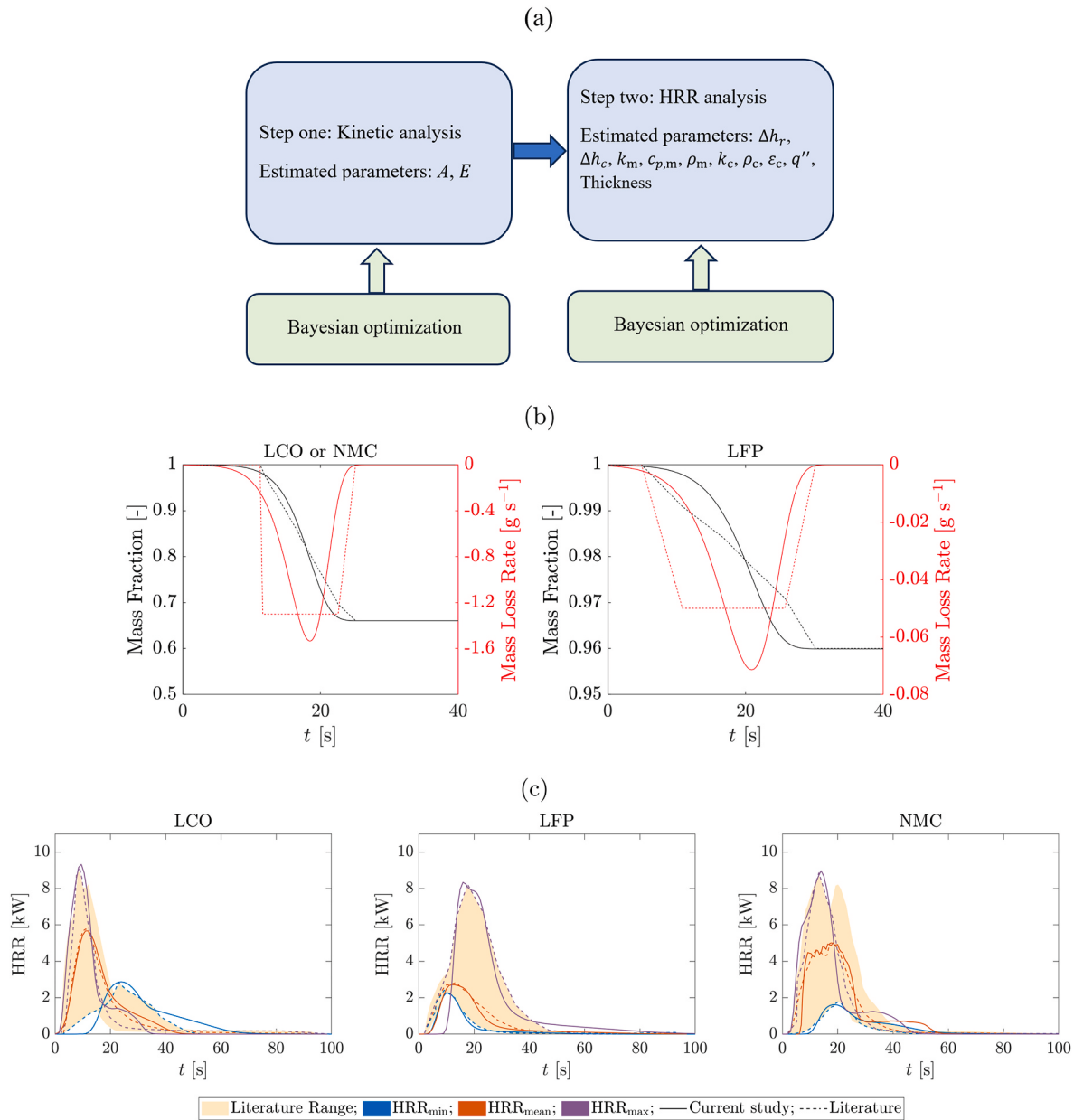


Fig. 2. The reported heat release rates for batteries with LCO, LFP and NMC cathodes in Said [31], Chen et al. [12], Fu et al. [13] and Wang et al. [32].



**Fig. 3.** (a) Pyrolysis parameter estimation performed in the current study. (b) Results of step one: mass fraction and mass loss rate of the current study (solid line) and Said [31] (dashed line) with LCO, NMC and LFP cathodes. (c) Results of step two: heat release rates obtained in the current study (solid line) compared to the experimental data of the literature (dashed line) with LCO, LFP and NMC cathodes.

**Table 3**

Estimated parameters used in the simulations. The subscripts  $c$  and  $m$  refer to char and material, respectively.

	LCO <sub>min</sub>	LCO <sub>mean</sub>	LCO <sub>max</sub>	LFP <sub>min</sub>	LFP <sub>mean</sub>	LFP <sub>max</sub>	NMC <sub>min</sub>	NMC <sub>mean</sub>	NMC <sub>max</sub>
$A [\times 10^8]$	1.87	1.87	1.87	1.52	1.52	1.52	1.87	1.87	1.87
$E [\times 10^5]$	1.0	1.0	1.0	1.0	1.0	1.0	1.0	1.0	1.0
$\Delta h_r$	114.2	114.2	114.2	114.2	114.2	114.2	114.2	843.7	114.21
$\Delta h_c [\times 10^5]$	0.2	0.189	0.189	1.1	2.0	6.0	0.189	0.17	0.189
$k_m$	0.1	0.1	0.1	0.1	0.1	0.1	0.1	0.1	0.1
$c_{p,m}$	1.14	1.14	1.14	1.14	1.14	1.14	1.14	1.70	1.14
$\rho_m$	739.5	739.5	739.5	739.5	739.5	739.5	739.5	635.3	739.5
$k_c$	0.36	0.36	0.36	0.36	0.36	0.36	0.36	0.30	0.36
$\rho_c$	251	251.0	251.0	30.0	30.0	30.0	251.0	216.0	251.0
$\varepsilon_c$	1.0	1.0	1.0	1.0	1.0	1.0	1.0	1.0	1.0
$q^a$	10.8	21.0	43.0	20.0	12.2	12.0	7.5	87.0	45.0
Thickness [ $\times 10^{-3}$ ]	1.5	2.0	2.5	1.0	1.0	1.0	0.8	3.25	3.3

<sup>a</sup>  $q''$  is the EXTERNAL\_FLUX in FDS terminology.

measurements.

### 3.2. Flame byproducts

Since the one-step combustion chemistry was employed in this work, it was needed to find the final amount of CO and soot values produced in the flame, as the byproducts. These values are defined as CO and soot yields as

$$y_{\text{CO}} = \frac{X_{\text{CO}} W_{\text{CO}}}{W_f} \quad (5)$$

$$y_{\text{soot}} = \frac{f_v W_s}{W_f} \quad (6)$$

respectively. In Eqs. Eq 4 and 5,  $X_{\text{CO}}$  and  $f_v$  are carbon monoxide mole fraction and soot volume fraction, respectively, and  $W_f$ ,  $W_s$  and  $W_{\text{CO}}$  are fuel, soot and CO molar weights, respectively.  $y_{\text{CO}}$  and  $y_{\text{soot}}$  are usually measured experimentally but there are limited works investigated these values for LIBs in the literature. Sun et al. [35] measured the toxic gases including CO emitted from pouch and 18650-type cells at 100% SOC. For the 18650-type cell, the amount of CO emission with LCO, NMC and LFP were 671 ppm, 616 ppm and 912 ppm, respectively [35]. To obtain  $X_{\text{CO}}$ , the values in ppm (part per million) were multiplied by  $10^{-6}$ .

Since no proper values were found in the literature for soot yield, a 1-D diffusion combustion of the vent gases, represented in Table 1, and Air was simulated using Cantera open-source solver [36] with the up-to-date version of CRECK detailed kinetics mechanism [28]. In these simulations, equivalence ratio is defined as

$$\varphi = \frac{m_f/m_o}{(m_f/m_o)_{\text{st}}} \quad (7)$$

where  $m_f$  and  $m_o$  are fuel and oxidizer masses and subscript "st" refers to the stoichiometric condition. The current 1-D flame simulations were performed for  $0.1 < \varphi < 2$ ,  $300 \text{ K} < T_f < 2000 \text{ K}$  and  $T_o = 300 \text{ K}$  where  $T_f$  and  $T_o$  are fuel and oxidizer temperatures, respectively. The details about soot modelling in CRECK mechanism is explained in section 2 of [28].

So far, soot volume fraction can be achieved for the specified range of  $\varphi$  and  $T_f$  but, the actual values of  $\varphi$  and  $T_f$  should be specified to find the

exact amounts of soot yields. To obtain these values, one approach was to track the amount of other values such as  $\text{CO}/\text{CO}_2$  ratio. This ratio was reported for batteries with LCO, LFP and NMC cathodes at 100% SOC as 0.83 [18], 0.02 [37] and 0.6 [38], respectively. The contours of  $\text{CO}/\text{CO}_2$  ratio with the values corresponding to the vent gas combustion from literature (solid line) are shown in Fig. 4.

Then, the temperatures of the unburnt vent gases were considered as fuel temperature ( $T_f$ ) here and are represented in Table 4 for every cathode at 100% SOC. It should be noted that these temperatures were taken from the early stages of thermal runaway, when the battery safety valve opens, and should not be mistaken with the gas temperature during combustion which are considerably higher. As presented in Table 4, different temperature values have been measured for every cathode with considerable differences. Hence, three fuel temperatures of minimum, maximum and also mean, by averaging the values, were considered here.

Now, using the values of  $\text{CO}/\text{CO}_2$  ratio (the solid lines in the first row contours of Fig. 4),  $T_f$ , and finding the corresponding  $\varphi$  from  $\text{CO}/\text{CO}_2$  ratios, the amounts of soot volume fractions can be obtained from the Cantera simulations. Second row of Fig. 4 shows the soot volume fraction contours versus temperature and equivalence ratio, with three values specified for minimum, mean and maximum  $T_f$  for every cathode. Table 5 presents the amounts of soot volume fractions and soot yields, calculated from Eq. (5). Although,  $y_{\text{soot},\text{max}}$  is recommended for the fire safety investigations.

**Table 4**

Vent gas temperatures before ignition reported in the literature at 100% SOC.

Reference	Battery type	Cathode	$T_f$ [K]
Somandepalli et al. [39]	Pouch	LCO	593.10
Kennedy et al. [40]	Pouch	LCO	457.20
Fernandes et al. [41]	26650	LFP	416.50
Yuan et al. [15]	18650	LFP	548.15
Archibald et al. [42]	Prismatic	NMC	447.30
Liu et al. [43]	Prismatic	NMC	396.05
Yan et al. [44]	18650	NMC	433.15
Yuan et al. [15]	18650	NMC	517.15
Yuan et al. [15]	18650	NMC	586.15
Zhao et al. [45]	18650	NMC	442.58

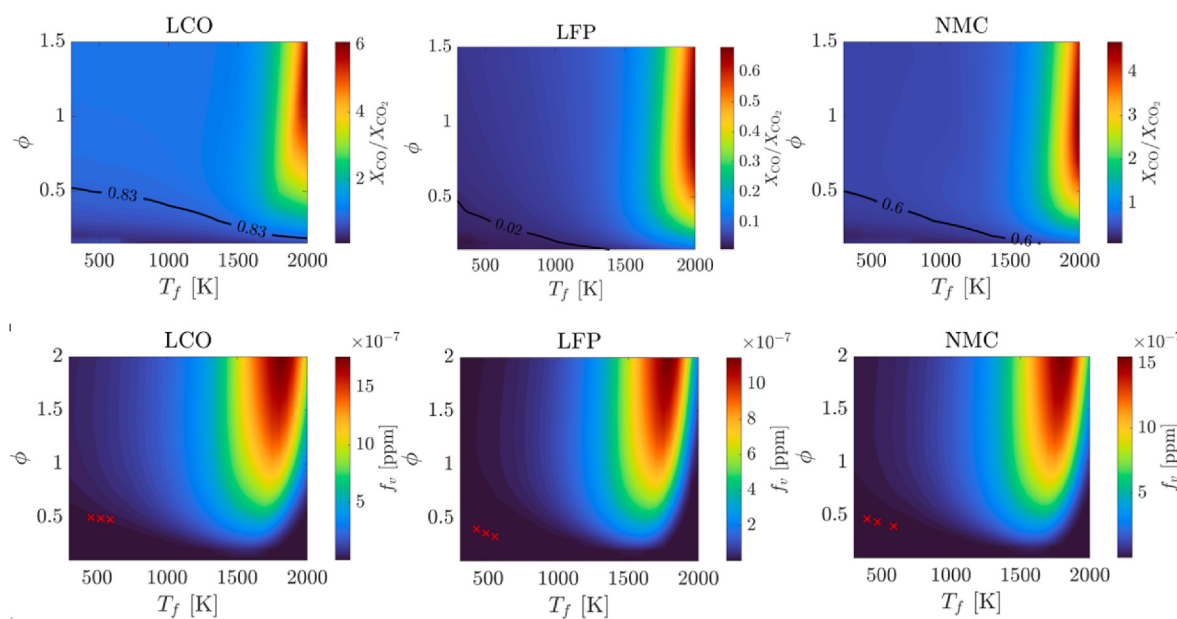


**Fig. 4.** First row: contours of  $\text{CO}/\text{CO}_2$  versus fuel temperature and equivalence ratio in 1-D combustion of the vent gases with LCO, LFP and NMC cathodes. Second row: contours of soot volume fraction versus fuel temperature and equivalence ratio in 1-D combustion of the battery vent gases with LCO, LFP and NMC cathodes. Cross marks indicate the values corresponding to the minimum, mean and maximum vent gas temperatures (fuel temperature).

**Table 5**

Soot volume fraction and soot yield calculated for the different vent gas temperatures.

Cathode	$f_v$	$y_{soot}$		
		Min	Mean	Max
LCO	$1.3 \times 10^{-8}$	$1.7 \times 10^{-8}$	$2.2 \times 10^{-8}$	$3.4 \times 10^{-8}$
	$6 \times 10^{-13}$	$2 \times 10^{-12}$	$5 \times 10^{-12}$	$5.2 \times 10^{-12}$
NMC	$1.2 \times 10^{-9}$	$1.4 \times 10^{-9}$	$1.6 \times 10^{-9}$	$3.1 \times 10^{-9}$
	$10^{-9}$	$10^{-9}$	$10^{-9}$	$10^{-9}$

The pyrolysis models, soot and CO yields obtained in this section were then used to analyse the flame and combustion properties in the next sections.

#### 4. Simulation of the battery flame

3-D simulations using the battery cell shown in Fig. 1, the estimated parameters presented in Table 3, and CO and soot yields discussed in section 3.2 are investigated in this section. Here, the computational domain was a  $0.2 \times 0.2 \times 1 \text{ m}^3$  cube. The 0.2 m size was previously validated in Ref. [16] and the 1 m height was found here to be tall enough to capture the flame completely. The ambient conditions were set at the top and side walls of the domain. The domain was closed at the bottom and cement properties from Ref. [46] were used for it as a material which has a low contribution to the gas-phase heat transfer and is not flammable. The simulation geometry is shown in Supplementary Material, Appendix A.

##### 4.1. Mesh independence

A mesh independence study was performed for the 3-D simulations. Here, four different meshes of M1, M2, M3 and M4 were created with the properties presented in Table 6. In all the cases, the domain was divided into 24 sub-meshes and the finest meshes were around and top of the battery which is called flame mesh in Table 6. The cell sizes were increased radially from the flame mesh by a ratio of 2:1.

The four cases were simulated with FDS at an arbitrary constant HRR of 9 kW (maximum HRR of LCO<sub>max</sub> presented in Table 2). The time-averaged gas temperature values at  $z = 0.2 \text{ m}$  were compared and the mean absolute differences between M1 and M2, M2 and M3 and M3 and M4 were 24.41 %, 6.85 % and 0.24 %. The mesh independence study is presented in more detail in Figure S2 of the Supplementary Material, Appendix A. Accordingly, making the mesh finer had significant effects on the temperature values up to M3 and then, the changes were not considerable with M4. Thus, mesh M3 was used here for all the 3-D simulations. In FDS, time step sizes are adjusted automatically so that the Courant- Friedrichs- Lewy (CFL) condition is satisfied. The procedure is explained in section 6.2.2 of FDS user's guide [30]. This default setting was followed here.

##### 4.2. Scalar fields

Fig. 5 shows the temperature scalar fields with LCO, LFP and NMC cathodes at different stages of the flame, with the maximum soot yield

**Table 6**

Properties of the meshes created for mesh independence study.

Mesh	Cell size in the flame mesh [mm]	Total number of cells
M1	4.0	231546
M2	2.0	458608
M3	1.0	988543
M4	0.5	2222720

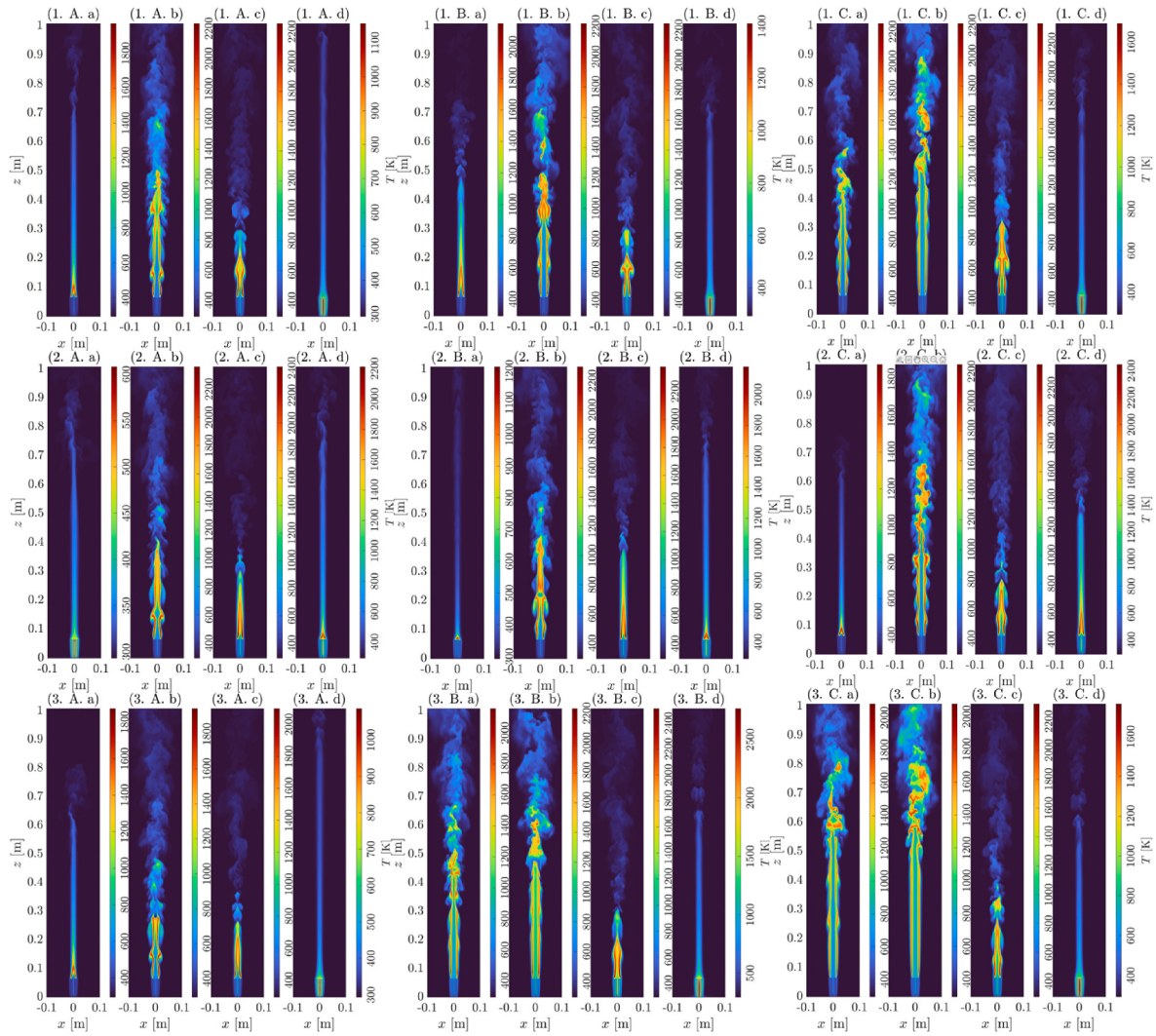
from Table 5. As expected, the temperature values were higher at the flame front where fuel and air mix with each other and combustion occurs. In the middle of the flame, i.e.,  $x = 0 \text{ m}$ , the temperature at higher elevations was higher due to buoyancy forces [47]. As seen, the flame temperature varied with HRR. For LCO<sub>min</sub>, the maximum temperatures at  $0.5t_{\text{HRR}_{\max}}$ ,  $t_{\text{HRR}_{\max}}$ ,  $2t_{\text{HRR}_{\max}}$ ,  $4t_{\text{HRR}_{\max}}$  were 1978 K, 2242 K, 2263 K and 1161 K, respectively, where  $t_{\text{HRR}_{\max}}$  refers to the time at which the HRR reached its maximum. This happened due to the different mixing rates at every stage and the amount of ejected gas. That is, at  $0.5t_{\text{HRR}_{\max}}$  the gas velocity was low, leading to low fuel/Air mixing. Increasing the HRR, the ejected gas at  $t_{\text{HRR}_{\max}}$  and flame temperature increased. At  $2t_{\text{HRR}_{\max}}$ , since the HRR was lower than that at  $t_{\text{HRR}_{\max}}$ , the amount of ejected fuel was lower but, the lower velocity of the ejected fuel prevented flame from extinguishing, resulted in higher flame temperatures. Then, as the HRR decreased at  $4t_{\text{HRR}_{\max}}$ , the flame temperature decreased. This analysis is applied to other cases, as well. In overall, the maximum flame temperature achieved with LCO, LFP and NMC cathodes were 2352 K, 2457 K and 2520 K, respectively.

Fig. 6 shows the scalar fields of CO<sub>2</sub>, H<sub>2</sub>O, CO, soot and velocity for different cathodes with maximum HRR, at  $y_{s,\max}$  from Table 5 and at  $t_{\text{HRR}_{\max}}$ . It was at the flame front, where the combustion reactions happen, CO<sub>2</sub> and H<sub>2</sub>O had the highest concentrations, as expected. With LCO, LFP and NMC cathodes, CO<sub>2</sub> mole fractions reached 0.25, 0.47 and 0.41 mol/mol<sub>mix</sub>, respectively, and H<sub>2</sub>O mole fractions were up to 0.14, 0.13 and 0.15 mol/mol<sub>mix</sub>, respectively. Besides, unlike other species, H<sub>2</sub>O concentration was not equal to zero outside the flame which corresponded to the air moisture. Due to the CO ejection and its production, it is seen that it had a considerable concentration in the flame up to 0.27, 0.30 and 0.13 mol/mol<sub>mix</sub> with LCO, LFP and NMC cathodes. Soot is another product which had the highest concentration at the flame front up to  $2.82 \times 10^{-8}$ ,  $3.46 \times 10^{-9}$  and  $2.61 \times 10^{-9}$  with LCO, LFP and NMC cathodes, respectively. The velocity scalar fields are also shown in Fig. 6. The maximum velocities achieved for the cases with LCO<sub>max</sub>, LFP<sub>max</sub> and NMC<sub>max</sub>, and they were 8.22 m/s, 5.77 m/s and 10.08 m/s, respectively. In some cases, e.g., 1. A. e and 2. B. e, it is seen that the velocity had the maximum values not at the cell ejecting area, but at higher elevations, around  $z = 2.5 \text{ m}$  which is because of the buoyancy forces. However, this phenomenon is rarely seen for the cases with HRR<sub>max</sub>, e.g., 1. C. e and 3. C. e. It is also seen that the soot yield could affect the gas velocity, however marginal. For instance, in the case LFP<sub>min</sub>, the maximum velocity was 5.58 m/s with  $y_{s,\min}$  however, 5.82 m/s was obtained with  $y_{s,\max}$ . This was mainly caused by the hot soot particles which increased the buoyancy forces and the gas dynamics. Further plots are presented in Appendix A, section 2 (Figures S.2- S. 19), to expand the individual scalar fields in more detail.

##### 4.3. Flame height

Determining flame height is necessary for understanding the interaction of the flame with its surroundings such as ceiling of a compartment or estimating the amount of radiative heat emitted by the flame [47]. However, the flame heights previously reported in the literature for 18650-type batteries, such as in Ref. [11], were not calculated based on heat release rates verified with experiments.

There are different approaches for calculating the flame height whether based on the flame temperature or the species concentrations. Here, the flame height was obtained by finding the axial location of the average peak centre-line temperature for every second with 0.1 s time intervals [48]. Fig. 7 shows the flame heights calculated for all the cases in Table 3 with heat release rates reported in Fig. 3. It is seen in Fig. 7 that the peak flame height varied between 0.42 m and 0.62 m, 0.29 m and 0.57 m, and 0.30 m and 0.60 m with LCO, LFP and NMC cathodes, respectively. As seen, the flame height strongly depends on the HRR. At higher HRRs, the mass flow rate of the vent gas (or the vent gas speed) was higher, leading to higher flame heights and due to the lower fuel



**Fig. 5.** Temperature scalar fields of 1. LCO, 2. LFP, 3. NMC, (A)  $HRR_{min}$ , (B)  $HRR_{mean}$ , (C)  $HRR_{max}$ , (a)  $0.5t_{HRR_{max}}$ , (b)  $t_{HRR_{max}}$ , (c)  $2t_{HRR_{max}}$  and (d)  $4t_{HRR_{max}}$ .

mass flow rate at lower HRRs, the flame heights were lower.

#### 4.4. Radiative heat flux

Due to high temperatures in fire scenarios, the radiative heat flux has a considerable contribution to the total heat transfer which accelerates the fire spread [49]. Accordingly, radiative heat flux could be important in thermal runaway propagation. Here, the computational domain was extended 1 m in  $x$ -direction and 100 measuring points were placed uniformly at  $z = 0.065$  m, the same height as an 18650-type cell. Additionally, 32 measuring points were placed on the battery surface to measure the feedback radiative heat flux to the cell surface. Fig. 8 shows the time-averaged radiative heat flux reaching the cell surface and the surroundings from the flame. As seen, the heat flux was significantly higher next to the cell and dramatically decreased at further distances until  $x = 0.2$  m where it vanished. The maximum radiative heat fluxes reaching the surroundings with LCO, LFP and NMC cathodes were  $6.68 \text{ kW/m}^2$ ,  $10.07 \text{ kW/m}^2$  and  $13.29 \text{ kW/m}^2$ , respectively, while radiation reaching the cell surface did not exceed  $1.39 \text{ kW/m}^2$ ,  $3.25 \text{ kW/m}^2$  and  $2.78 \text{ kW/m}^2$ , respectively. The radiative heat flux incident on the cell surface was considerably lower than that to the surroundings, which is due to the small view factor between the flame and the cell surface. To compare the heat flux on the surface and surroundings,  $R = \dot{q}_{r,surr}''/\dot{q}_{r,surf}''$  is defined here where the subscripts "surr" and "surf" refer to

surroundings and battery surface, respectively. It is seen in Fig. 8 that  $\dot{q}_{r,surr}''$  next to the cell, depending on the HRR, was 1.8–12.4 times greater than  $\dot{q}_{r,surf}''$ , meaning that the radiative heat flux affected surrounding area more than the cell surface. As expected, the radiative heat flux was higher at higher HRR and increased by increasing soot yield due to the higher radiative emission from the flame.

## 5. Conclusion

The flame properties and hazards of an 18650-type LIB cell, during thermal runaway, with LCO, LFP and NMC cathodes at 100% SOC were studied here. The flaming process of the battery cell was assumed to behave like a pyrolysis process with a single-step kinetic. The kinetic and thermal properties parameters were obtained by fitting the modelling results to the experimental measurements. The novelties of the current approach are that for simulating the battery flame, there is no need to model the mechanisms prior to flaming and, the resulting flame heat release rate is experimentally verified.

Since one-step kinetic was assumed for combustion, the CO yield measured in the literature was employed and the soot yield was obtained from 1-D diffusion flame simulations. The gas temperature, species concentrations, gas velocity, flame height and radiative heat flux were reported for each case. The results indicated that due to the ejection of CO and  $\text{CO}_2$ , these species had a considerable contribution to the flame

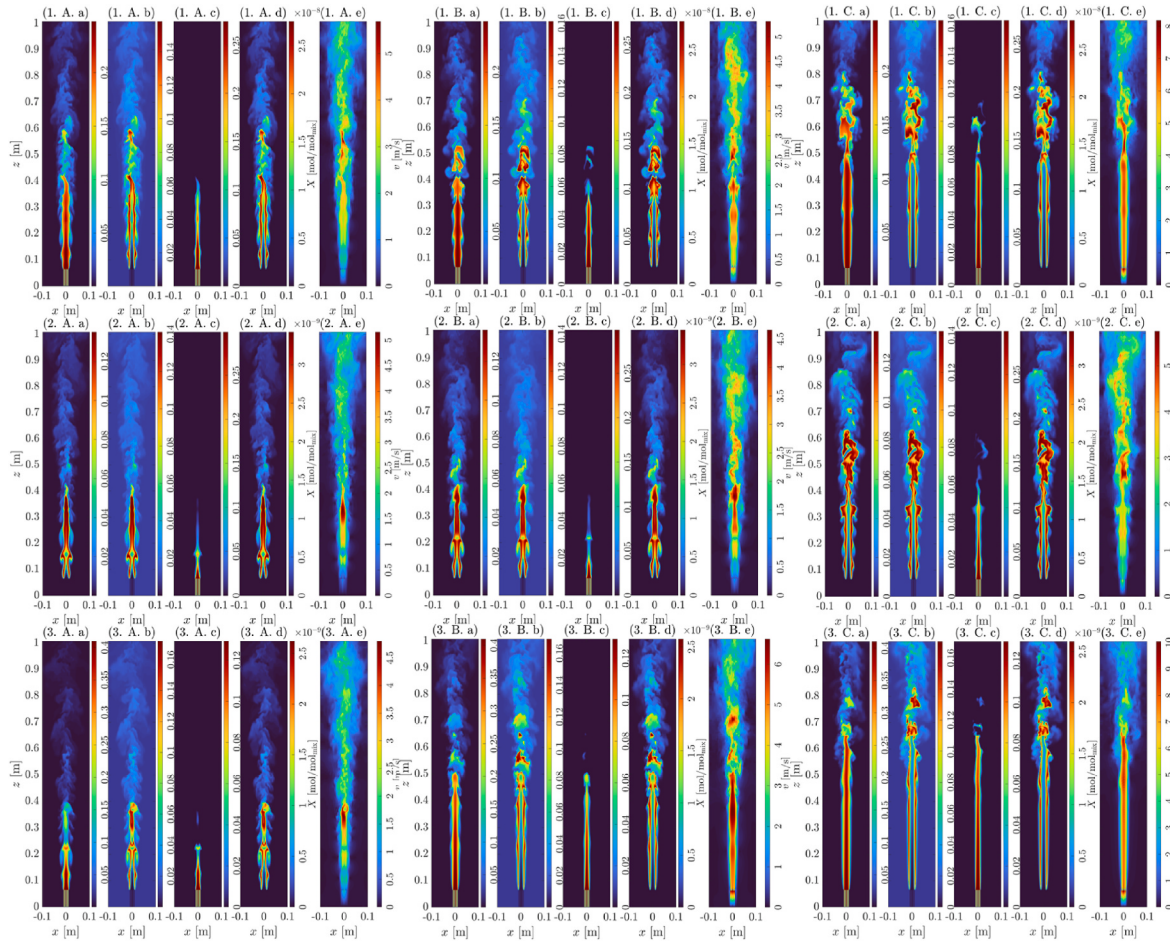


**Fig. 6.** Scalar fields of 1. LCO, 2. LFP, 3. NMC, (A)  $HRR_{min}$ , (B)  $HRR_{mean}$ , (C)  $HRR_{max}$ , (a)  $\text{CO}_2$ , (b)  $\text{H}_2\text{O}$ , (c)  $\text{CO}$ , (d) soot and (e) velocity at  $t_{HRR_{max}}$ .

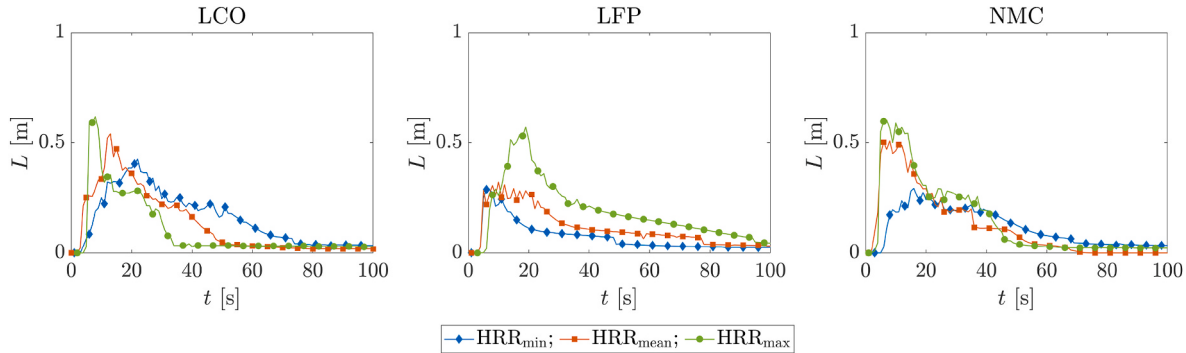


**Fig. 7.** The flame heights calculated based on the flame simulations with minimum, mean and maximum heat release rates and with LCO, LFP and NMC cathodes.

with mole fractions up to  $X_{\text{CO}} = 0.3$  and  $X_{\text{CO}_2} = 0.47$  with LFP cathode. They were found not only at the flame front, but also inside the flame. These observations could be useful in future studies of battery fires when considering combustion and radiative heat transfer modelling. As calculated, the flame height could reach 0.62 m, 0.57 m and 0.60 m with  $\text{LCO}_{\text{max}}$ ,  $\text{LFP}_{\text{max}}$  and  $\text{NMC}_{\text{max}}$ , respectively, and the minimum flame heights were 0.42 m, 0.29 m and 0.30 m for  $\text{LCO}_{\text{min}}$ ,  $\text{LFP}_{\text{min}}$  and  $\text{NMC}_{\text{min}}$ , respectively. The maximum radiative heat flux was observed at the distance of 0.001 m from the cell, at 6.68 kW/m<sup>2</sup>, 10.07 kW/m<sup>2</sup> and 13.29 kW/m<sup>2</sup> for  $\text{LCO}_{\text{max}}$ ,  $\text{LFP}_{\text{max}}$  and  $\text{NMC}_{\text{max}}$ , respectively. However, the feedback heat flux to the cell surface was much lower than these values, which indicated that radiative heat flux contributed more to thermal runaway propagation than surface heating. It was also observed

that the higher soot yield led to higher radiative heat fluxes which is due to the higher radiative emissions in the flame. These results are novel as they were obtained from simulations with experimentally verified HRRs.

Overall, the generated pyrolysis models offer a straightforward approach for modelling 18650-type lithium-ion battery fires in thermal runaway. In contrast to previous studies, the current methodology eliminates coupling various solutions for flame simulations, resulting in experimentally verified flame heat release rates and thus, valid flame properties. This work can be built on in the future both with more complex pyrolysis kinetics and can be applied to different battery types.

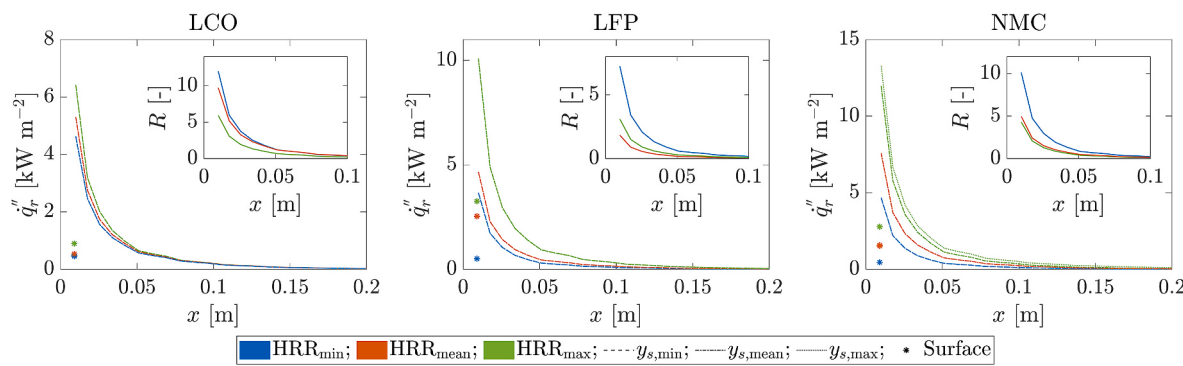


**Fig. 8.** Radiative heat flux reaching the cell surface and the surroundings with LCO, LFP and NMC cathodes and different soot yields.

## CRediT authorship contribution statement

**Hosein Sadeghi:** Writing – original draft, Methodology, Investigation, Formal analysis, Data curation, Conceptualization. **Francesco Restuccia:** Writing – review & editing, Writing – original draft, Supervision, Project administration, Methodology, Funding acquisition, Formal analysis, Conceptualization.

## Declaration of competing interest

The authors declare that they have no known competing financial interests or personal relationships that could have appeared to influence the work reported in this paper.

## Data availability

Data will be made available on request.

## Acknowledgements

This work was supported by King's College London NMES Ph.D. scholarship and by the Faraday Institution [grant number FIRG061]. The computational resources were provided by King's Computational Research, Engineering and Technology Environment (CREATE).

## Appendix A. Supplementary data

Supplementary data to this article can be found online at <https://doi.org/10.1016/j.jpowsour.2024.234480>.

## References

- [1] Q. Wang, B. Mao, S.I. Stoliarov, J. Sun, A review of lithium ion battery failure mechanisms and fire prevention strategies, *Prog. Energy Combust. Sci.* 73 (2019) 95–131, <https://doi.org/10.1016/j.pecs.2019.03.002>.
- [2] J.W. Fergus, Recent developments in cathode materials for lithium ion batteries, *J. Power Sources* 195 (4) (2010) 939–954, <https://doi.org/10.1016/j.jpowsour.2009.08.089>.
- [3] H. Wang, et al., Fire and explosion characteristics of vent gas from lithium-ion batteries after thermal runaway: a comparative study, *eTransportation* (2022) 100190, <https://doi.org/10.1016/j.etrans.2022.100190>.
- [4] G. Hu, P. Huang, Z. Bai, Q. Wang, K. Qi, Comprehensively analysis the failure evolution and safety evaluation of automotive lithium ion battery, *eTransportation* 10 (2021) 100140, <https://doi.org/10.1016/j.etrans.2021.100140>.
- [5] A.W. Golubkov, et al., Thermal-runaway experiments on consumer Li-ion batteries with metal-oxide and olivine-type cathodes, *RSC Adv.* 4 (7) (2014) 3633–3642, <https://doi.org/10.1039/C3RA45748F>.
- [6] A.R. Baird, E.J. Archibald, K.C. Marr, O.A. Ezekoye, Explosion hazards from lithium-ion battery vent gas, *J. Power Sources* 446 (2020) 227257, <https://doi.org/10.1016/j.jpowsour.2019.227257>.
- [7] O. Mathieu, C.M. Grégoire, M.A. Turner, D.J. Mohr, S.A. Alturaiif, J.C. Thomas, E. L. Petersen, Experimental investigation of the combustion properties of an average thermal runaway gas mixture from Li-ion batteries, *Energy Fuel.* 36 (6) (2022) 3247–3258, <https://doi.org/10.1021/acs.energyfuels.1c04057>.
- [8] M. Henriksen, K. Vågsæther, J. Lundberg, S. Forseth, D. Bjerkevold, Laminar burning velocity of gases vented from failed Li-ion batteries, *J. Power Sources* 506 (2021) 230141, <https://doi.org/10.1016/j.jpowsour.2021.230141>.
- [9] M. Henriksen, K. Vågsæther, J. Lundberg, S. Forseth, D. Bjerkevold, Explosion characteristics for Li-ion battery electrolytes at elevated temperatures, *J. Hazard Mater.* 371 (2019) 1–7, <https://doi.org/10.1016/j.jhazmat.2019.02.108>.
- [10] J. Johnsplass, M. Henriksen, K. Vågsæther, J. Lundberg, D. Bjerkevold, Simulation of burning velocities in gases vented from thermal run-a-way lithium ion batteries. <https://doi.org/10.3384/ecp17138157>, 2017.
- [11] B. Mao, C. Zhao, H. Chen, Q. Wang, J. Sun, Experimental and modeling analysis of jet flow and fire dynamics of 18650-type lithium-ion battery, *Appl. Energy* 281 (2021) 116054, <https://doi.org/10.1016/j.apenergy.2020.116054>.
- [12] M. Chen, D. Zhou, X. Chen, W. Zhang, J. Liu, R. Yuen, J. Wang, Investigation on the thermal hazards of 18650 lithium ion batteries by fire calorimeter, *J. Therm. Anal. Calorim.* 122 (2) (2015) 755–763, <https://doi.org/10.1007/s10973-015-4751-5>.
- [13] Y. Fu, S. Lu, K. Li, C. Liu, X. Cheng, H. Zhang, An experimental study on burning behaviors of 18650 lithium ion batteries using a cone calorimeter, *J. Power Sources* 273 (2015) 216–222, <https://doi.org/10.1016/j.jpowsour.2014.09.039>.
- [14] X. Liu, S.I. Stoliarov, M. Denlinger, A. Masias, K. Snyder, Comprehensive calorimetry of the thermally-induced failure of a lithium ion battery, *J. Power Sources* 280 (2015) 516–525, <https://doi.org/10.1016/j.jpowsour.2015.01.125>.
- [15] L. Yuan, T. Dubaniwicz, I. Zlochower, R. Thomas, N. Rayyan, Experimental study on thermal runaway and vented gases of lithium-ion cells, *Process Saf. Environ. Protect.* 144 (2020) 186–192, <https://doi.org/10.1016/j.psep.2020.07.028>.
- [16] D. Kong, G. Wang, P. Ping, J. Wen, A coupled conjugate heat transfer and CFD model for the thermal runaway evolution and jet fire of 18650 lithium-ion battery under thermal abuse, *eTransportation* 12 (2022) 100157, <https://doi.org/10.1016/j.etrans.2022.100157>.
- [17] X. Liu, Z. Wu, S.I. Stoliarov, M. Denlinger, A. Masias, K. Snyder, Heat release during thermally-induced failure of a lithium ion battery: impact of cathode composition, *Fire Saf. J.* 85 (2016) 10–22, <https://doi.org/10.1016/j.firesaf.2016.08.001>.
- [18] M. Chen, J. Liu, Y. He, R. Yuen, J. Wang, Study of the fire hazards of lithium-ion batteries at different pressures, *Appl. Therm. Eng.* 125 (2017) 1061–1074, <https://doi.org/10.1016/j.applthermaleng.2017.06.131>.
- [19] A. García, J. Monsalve-Serrano, R.L. Sari, S. Martínez-Boggio, Influence of environmental conditions in the battery thermal runaway process of different chemistries: thermodynamic and optical assessment, *Int. J. Heat Mass Tran.* 184 (2022) 122381, <https://doi.org/10.1016/j.ijheatmasstransfer.2021.122381>.
- [20] Z. Wang, D. Ouyang, M. Chen, X. Wang, Z. Zhang, J. Wang, Fire behavior of lithium-ion battery with different states of charge induced by high incident heat fluxes, *J. Therm. Anal. Calorim.* 136 (6) (2019) 2239–2247, <https://doi.org/10.1007/s10973-018-7899-y>.
- [21] Q. Zhang, T. Liu, Q. Wang, Experimental study on the influence of different heating methods on thermal runaway of lithium-ion battery, *J. Energy Storage* 42 (2021) 103063, <https://doi.org/10.1016/j.est.2021.103063>.
- [22] J. Kim, A. Mallarapu, D.P. Finegan, S. Santhanagopalan, Modeling cell venting and gas-phase reactions in 18650 lithium ion batteries during thermal runaway, *J. Power Sources* 489 (2021) 229496, <https://doi.org/10.1016/j.jpowsour.2021.229496>.
- [23] Y. Takagishi, Y. Tozuka, T. Yamanaka, T. Yamaue, Heating simulation of a Li-ion battery cylindrical cell and module with consideration of gas ejection, *Energy Rep.* 8 (2022) 3176–3188, <https://doi.org/10.1016/j.egyr.2022.02.086>.
- [24] P. Zhang, J. Lu, K. Yang, H. Chen, Y. Huang, A 3D simulation model of thermal runaway in Li-ion batteries coupled particles ejection and jet flow, *J. Power Sources* 580 (2023) 233357.
- [25] A. Viitanen, S. Hostikka, J. Vaari, CFD simulations of fire propagation in horizontal cable trays using a pyrolysis model with stochastically determined geometry, *Fire Technol.* 58 (5) (2022) 3039–3065, <https://doi.org/10.1007/s10694-022-01291-6>.
- [26] R. Kallada Janardhan, S. Hostikka, Predictive computational fluid dynamics simulation of fire spread on wood cribs, *Fire Technol.* 55 (6) (2019) 2245–2268, <https://doi.org/10.1007/s10694-019-00855-3>.
- [27] G. Zhong, H. Li, C. Wang, K. Xu, Q. Wang, Experimental analysis of thermal runaway propagation risk within 18650 lithium-ion battery modules,

- J. Electrochem. Soc. 165 (9) (2018) A1925, <https://doi.org/10.1149/2.0461809jes>.
- [28] A. Nobili, A. Cuoci, W. Pejpichertakul, M. Pelucchi, C. Cavallotti, T. Faravelli, Modeling soot particles as stable radicals: a chemical kinetic study on formation and oxidation. Part I. Soot formation in ethylene laminar premixed and counterflow diffusion flames, Combust. Flame 243 (2022) 112073, <https://doi.org/10.1016/j.combustflame.2022.112073>.
- [29] T. Sikanen, S. Hostikka, Numerical simulations of liquid spreading and fires following an aircraft impact, Nucl. Eng. Des. 318 (2017) 147–162, <https://doi.org/10.1016/j.nucengdes.2017.04.012>.
- [30] K. McGrattan, S. Hostikka, R. McDermott, J. Floyd, C. Weinschenk, K. Overholz, Fire dynamics simulator user's guide, NIST Spec. Publ. 1019 (6) (2013) 1–339.
- [31] A.O. Said, Dynamics and Hazards of Cascading Failure in Lithium Ion Cell Arrays: Analysis, Passive Mitigation, and Active Suppression, University of Maryland, College Park, 2020.
- [32] W. Wang, T. He, S. He, T. You, F. Khan, Modeling of thermal runaway propagation of NMC battery packs after fast charging operation, Process Saf. Environ. Protect. 154 (2021) 104–117, <https://doi.org/10.1016/j.psep.2021.08.006>.
- [33] M. Pelikan, D.E. Goldberg, E. Cantú-Paz, BOA: the Bayesian optimization algorithm, in: Proceedings of the Genetic and Evolutionary Computation Conference GECCO-99 vol. 1, Citeseer, 1999, 1999.
- [34] S.I. Stoliarov, J. Li, Parameterization and validation of pyrolysis models for polymeric materials, Fire Technol. 52 (2016) 79–91, <https://doi.org/10.1007/s10694-015-0490-1>.
- [35] J. Sun, et al., Toxicity, a serious concern of thermal runaway from commercial Li-ion battery, Nano Energy 27 (2016) 313–319, <https://doi.org/10.1016/j.nanoen.2016.06.031>.
- [36] D.G. Goodwin, H.K. Moffat, R.L. Speth, Cantera: an Object-Oriented Software Toolkit for Chemical Kinetics, Thermodynamics, and Transport Processes, Cantera Developers, Warrendale, IL, 2017, version 2.2. 1.
- [37] Y. Peng, et al., A comprehensive investigation on the thermal and toxic hazards of large format lithium-ion batteries with LiFePO<sub>4</sub> cathode, J. Hazard Mater. 381 (2020) 120916, <https://doi.org/10.1016/j.jhazmat.2019.120916>.
- [38] D. Ouyang, M. Chen, J. Wang, Fire behaviors study on 18650 batteries pack using a cone-calorimeter, J. Therm. Anal. Calorim. 136 (6) (2019) 2281–2294, <https://doi.org/10.1007/s10973-018-7891-6>.
- [39] V. Somandepalli, K. Marr, Q. Horn, Quantification of combustion hazards of thermal runaway failures in lithium-ion batteries, SAE Int. J. Alternative Powertrains 3 (1) (2014) 98–104, <https://doi.org/10.4271/2014-01-1857>.
- [40] R.W. Kennedy, K.C. Marr, O.A. Ezekoye, Gas release rates and properties from Lithium Cobalt Oxide lithium ion battery arrays, J. Power Sources 487 (2021) 229388, <https://doi.org/10.1016/j.jpowsour.2020.229388>.
- [41] Y. Fernandes, A. Bry, S. De Persis, Identification and quantification of gases emitted during abuse tests by overcharge of a commercial Li-ion battery, J. Power Sources 389 (2018) 106–119, <https://doi.org/10.1016/j.jpowsour.2018.03.034>.
- [42] E.J. Archibald, Fire & Explosion Hazards Due to Thermal Runaway Propagation in Lithium-Ion Battery Systems, 2021.
- [43] P. Liu, et al., Experimental study on the thermal runaway and fire behavior of LiNi0.8Co0.1Mn0.1O2 battery in open and confined spaces, Process Saf. Environ. Protect. 158 (2022) 711–726, <https://doi.org/10.1016/j.psep.2021.12.056>.
- [44] H. Yan, K.C. Marr, O.A. Ezekoye, Towards fire forensic characteristics of failed cylindrical format lithium-ion cells and batteries, Fire Technol. 57 (4) (2021) 1723–1752, <https://doi.org/10.1007/s10694-020-01079-6>.
- [45] C. Zhao, J. Sun, Q. Wang, Thermal runaway hazards investigation on 18650 lithium-ion battery using extended volume accelerating rate calorimeter, J. Energy Storage 28 (2020) 101232, <https://doi.org/10.1016/j.est.2020.101232>.
- [46] M.J. Hurley, et al., SFPE Handbook of Fire Protection Engineering, Springer, 2015.
- [47] D. Drysdale, An Introduction to Fire Dynamics, John Wiley & Sons, 2011.
- [48] S.R. Turns, Introduction to Combustion, McGraw-Hill Companies, New York, NY, USA, 1996.
- [49] H. Sadeghi, S. Hostikka, G.C. Fraga, H. Bordbar, Weighted-sum-of-gray-gases models for non-gray thermal radiation of hydrocarbon fuel vapors, CH<sub>4</sub>, CO and soot, Fire Saf. J. 125 (2021) 103420, <https://doi.org/10.1016/jfiresaf.2021.103420>.